Chapter 2

Background

This chapter introduces some background relevant to the discussions in this dissertation. Section 2.1 is a brief introduction of the half-metal Fe_3O_4 including the structure, magnetic and electronic properties. Section 2.2 is a brief introduction of the dilute magnetic semiconductor (DMS) ZnCoO including the related theory. Section 2.3 is a summary of magnetoresistance, including the basic phenomenology and the theoretical models on tunneling magnetoresistance (TMR). Section 2.4 is a summary of magnetic coupling about the exchange coupling.

2.1. Half-metal Fe_3O_4

2.1.a Half Metal

A half metal would provide single spin conduction electron from Fermi surface. For the opposite spin there is a gap in the spin-polarized density of state, which was similar to the insulator. On the other words, this material has only one spin subband with partially occupied at the Fermi-level. Another spin subband was totally filled or empty and separated from the Fermi level by a band gap. Material such as Heusler alloy (NiMnSb), chromium dioxides (CrO_2), pervoskites ($La_{0.7}Sr_{0.3}MnO_3$) and magnetite (Fe_3O_4) are expected to be half-metallic and have been investigated for device application [1-6]. Heusler alloy has an ordered f.c.c. structure and its Curie temperature is 728K [1]. The complicated composition and requirement for the ordering phase was the main issue need to solve in Heusler alloy based MTJ. The simplest half metal is CrO_2, where an energy gap at the Fermi level is also in the minority density of states [2]. CrO_2 has a tetragonal rutile structure and its Curie temperature is 398K. Tunnel junctions with CrO_2 have shown MR below 1% at 77K [6]. LSMO have rhombohedral structure and its Curie temperature is 380K [2]. Tunnel junctions with LSMO have shown MR of 1800% which is the highest MR. However, the Curie temperature of these two materials is too low to be used in the conventional device. Magnetite (Fe_3O_4) which has inverse spinel structure and its Curie temperature is 850K. Fe_3O_4-based tunnel junctions revealed 14% MR at

room temperature. Due to the high Curie temperature of Fe_3O_4, it is most promising material for spintonic device. In this thesis, we will focus on the fabrication of the Fe_3O_4 thin film and Fe_3O_4-based magnetic tunnel junctions.

2.2.b Properties of Fe_3O_4

Magnetite or Fe_3O_4 is one of the most studied magnetic materials. The interest in Fe_3O_4 was from its high Curie temperature (T_C~850K), electrically conducting (conductivity~250$\Omega^{-1}cm^{-1}$), and high spin-polarization (half metal). Therefore, it was an ideal candidate for room temperature application. Fe_3O_4 has the cubic inverse spinel structure in which the Fe cations occupy interstices of a face-centered-cubic (FCC) close packed frame of oxygen ions. The eight tetrahedral (A) sites are occupied by Fe^{3+}, while the 16 octahedral (B) sites are equally shared by Fe^{3+} and Fe^{2+} ions. Within A or B sites, magnetic moments are aligned ferromagnetically. However, the moment between A and B sublattice are aligned antiferromagnetically. Since the moment in A sites and B sites are aligned antiferromagnetically, the moment of the Fe^{3+} ion will be canceled out, resulting in only Fe^{2+} remaining. Therefore, the net moment is 4 μ_B.

Rapid hoping of electron between Fe^{2+} and Fe^{3+} ions in the B site results in good room-temperature conductivity. The famous Verwey

transition is a metal to insulator transition. The mechanism of this transition is not well-understood. One of the possible reasons is that the electron hopping is frozen at the temperature close to 120K (T_V：Verwey temperature) [7]. T_V is the important characteristic of half-metallic Fe_3O_4. In the published papers of Fe_3O_4 thin films, Verwey transition close to 120 K was obtained by growing films directly on single-crystal substrates at high temperature [8-9].

2.1.c Fabrication and Identification of Fe_3O_4

In this section, we introduce deposition methods for Fe_3O_4 thin films, and compare the quality of the Fe_3O_4 films. Gong *et al*. [10] succeeded in obtaining M_S=~415 emu/ cm^3 and T_V=~120K on a MgO(100) substrate by using a pulsed laser deposition (PLD) system, but the deposition temperature was at 350℃, and the thickness was as thick as 6600Å. Figure 2.1 revealed the resistivity as a function of temperature for the 150 nm and 660 nm thick Fe_3O_4 films. T_V is determined to be about 120K for 660 nm Fe_3O_4 film. The transition temperature of thinner film is broader than that for the thicker film. This is possibly due to the residual strain in the films resulting from the lattice mismatch with the substrate.

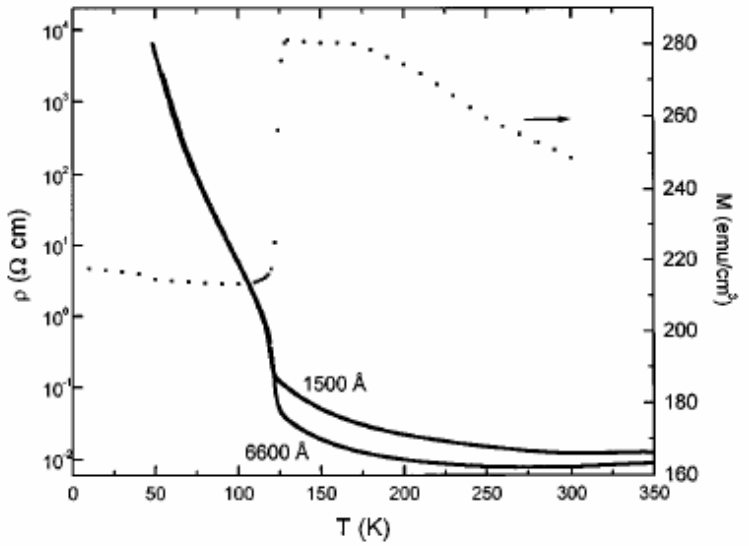

Fig. 2.1. The resistivity as a function of temperature for 150 nm and 660 nm thick Fe_3O_4 films in the range of 60~350K. The magnetization as a function of temperature is also shown for the 660 nm film measures in a field of 300 Oe [10].

Hong *et al.* [11] used a reactive rf sputtering system integrated with an external rf source to deposit Fe_3O_4 films at room temperature, the clear Verwey transition was observed at 125K. However, the M_S value of the polycrystalline films was only 190.6 emu/cm^3. X-ray photoelectron spectroscopy (XPS) measurements shown in Fig 2.2, which were performed in order to investigate the valence state of thin film, depending on whether the rf external power was applied during the film growth. The Fe 2*p* line shape in iron oxides is rather complex and a small amount of chemical shift between Fe^{2+} and Fe^{3+} components appears.

However, the satellite peaks (SAT) caused by charge transfer screening allow us to identify the Fe oxidation state. Figure 2.2 showed the typical Fe 2*p* core level spectra of the Fe_3O_4 films with an external

power and zero-external power, respectively. The films at an external rf power of 120W had no satellite peak at 718 eV. The observed spectra of the Fe_3O_4 thin films were well-matched to reference spectra of the Fe_3O_4. As shown in a dashed line, the spectra of the Fe_3O_4 films formed at zero-external power clearly exhibited a satellite peak between the Fe $2p^{3/2}$ and Fe $2p^{1/2}$ XPS spectrum of the films. The existence of a SAT peak in the XPS measurement at 718 eV is an evidence of the Fe_2O_3 phase formed in the Fe_3O_4 film under zero-external power growth. The origin of the SAT peak was expected due to the screening effect caused by a charge transfer process [11].

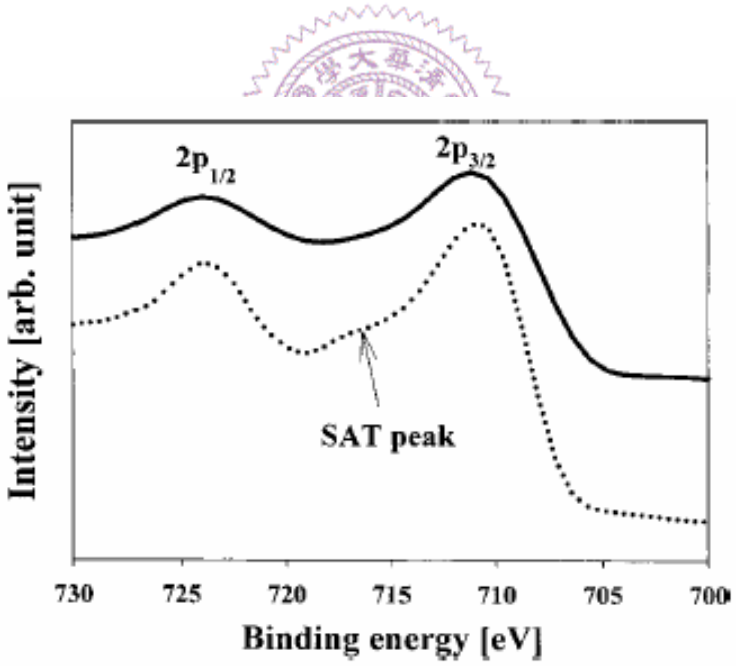

Fig. 2.2. Typical XPS measurement of Fe 2p core spectra of the Fe_3O_4 thin films prepared by external power of 120W (solid line) and zero-power (dashed line). [11]

Aoshima *et al.* [12] reported that the M_S of 430±50 emu/ cm^3 could be obtained on MgO (110) substrates grown at 350℃ by ion beam sputtering with a Fe_3O_4 target. However, the Verwey transition was not clearly observed, as shown in the Fig 2.3.

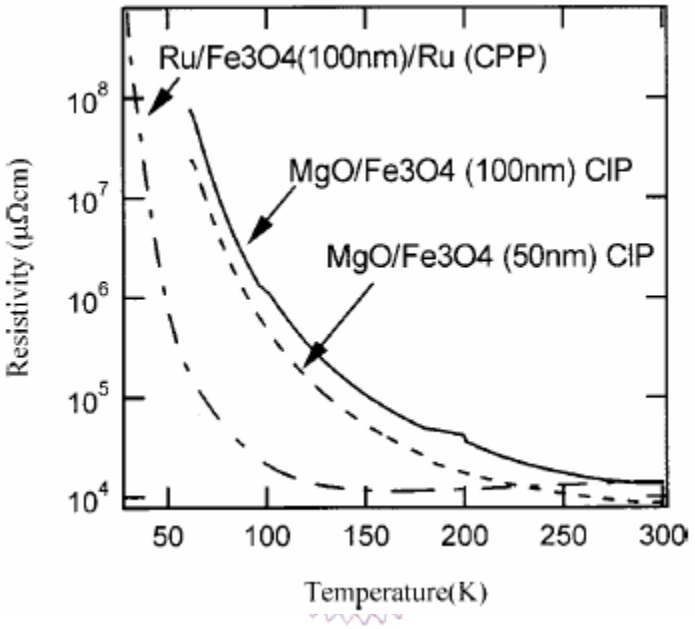

Fig. 2.3. Resitivity of the MgO/Fe_3O_4 films (50,100 nm), and of MgO/Ru/ Fe_3O_4 (100nm)/Ru (perpendicular to the plane direction). [12]

To take advantages of half-metallic films for spintronic devices, for example, TMR or GMR devices, low temperature deposition is preferred. In addition, epitaxial Fe_3O_4 films may enable us to clearly investigate the effects of the half metal without grain boundary scattering. Therefore, the main purpose of this work is to grow epitaxial Fe_3O_4 films at room temperature. We used reactive ion beam deposition (IBD) to grow Fe_3O_4.

Since the working pressure of IBD is 10^{-4} Torr, this low working pressure reduces the number of collisions between sputtered atoms and

gas ions. In addition, the beam voltage of the IBD system can be independently controlled regardless of working pressure and can be raised to 1500 V. Consequently, the IBD system can provide relativity high incident energy of sputtered atoms compared to other deposition method. The energy given by the ion beam system is high enough to reduce the temperature needed for the formation of the Fe_3O_4 phase.

2.3.d Fe_3O_4 Based MTJs [13]

Basically, scientists have searched one high spin polarization material with T_C much higher than room temperature, so that the magnetization and spin polarization would be coherent and stable at room temperature. One such magnetic oxide, for which 100% spin polarization has been reported, is Fe_3O_4. The T_C for this material is much higher than the room temperature (~850K) and hence Fe_3O_4 is expected to have very high spin polarization at room temperature.

The first MTJ type hetrostructure based on Fe_3O_4 was studied by Ghosh *et al*. [4] in the form of Fe_3O_4/STO/LSMO tri-layer device. The magnetotrnasport data measured at different temperatures were shown in Fig. 2.4. Significant MR was observed only below 200 K. The MR was composed of a positive sharp central MR feature at low field, and the tails at higher fields revealing a negative MR contribution to the total MR. The contribution of the positive MR increases with lowering the temperature. The MR results for the hetrostructure measured at 80 K were plotted in

Fig. 2.5 along with that for individual LSMO and Fe_3O_4 layers. Since the MR of LSMO and Fe_3O_4 was negative, the observed positive MR contribution has to be from the Fe_3O_4/STO/LSMO junction.

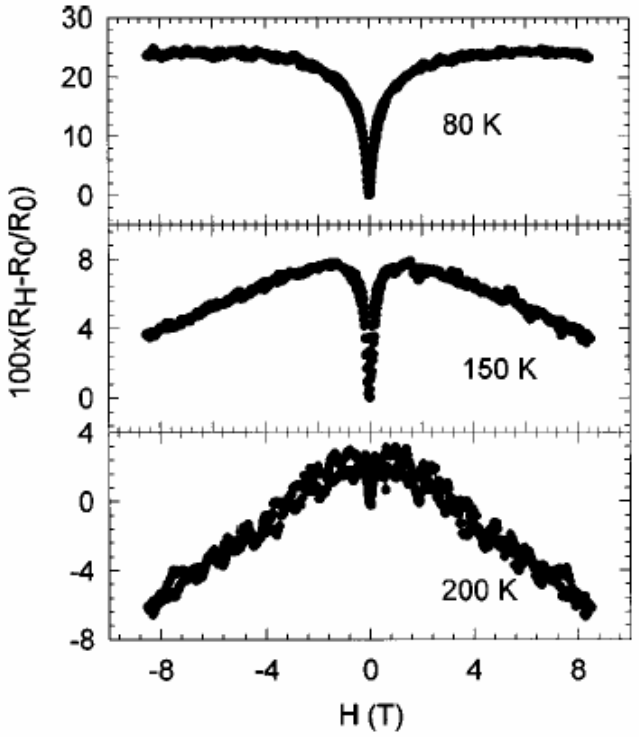

Fig. 2.4. Magnetoresistance as a function of the in-plane applied magnetic field at different temperature for the Fe_3O_4/STO/LSMO heterostructure [4].

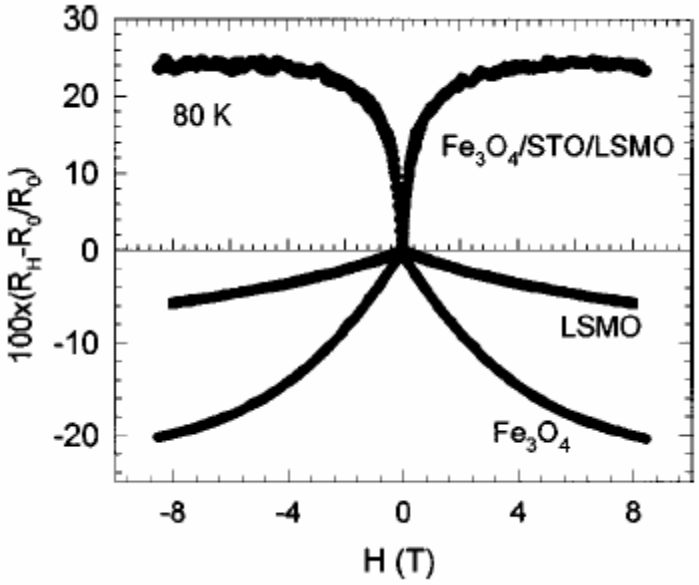

Fig. 2.5. Magnetoresistance as a function of the in-plane applied magnetic field at 80 K for the Fe_3O_4/STO/LSMO heterostructure and for the individual layers of Fe_3O_4 and LSMO layers [4].

The MR at 80 K could be separated into two region, one at lower field (H<0.5T) and the other at fields higher than 0.5 T. The hysteresis loop of the device measured at 80 K revealed two values of coercivity: 0.4 and 1 kOe corresponding to LSMO and Fe_3O_4 layers, respectively. Obviously, the MR data do not reveal any specific correlation with these two coercivity values. Furthermore, the observation of giant positive MR when the magnetizations of the two electrodes were parallel aligned by applying magnetic field is very interesting.

The full density of state near the Femi energy is contributed by the minority spin band (carrier spin, S^C anti-parallel to M) in Fe_3O_4, while the main contribution to density of state near Fermi energy is from the

majority spin band (S^C parallel to M) in LSMO. Therefore, the conducting electrons in Fe_3O_4 and LSMO have opposite spin orientation relative to the magnetization direction, as shown in the Fig. 2.6. The heterostructure revealed in the high resistance state with the magnetization of Fe_3O_4 and LSMO were parallel at high applied magnetic field. At low field, due to the canting of magnetization and domain formation, the magnetization in the two layers are no longer parallel and hence the resistance of the junction is lower.

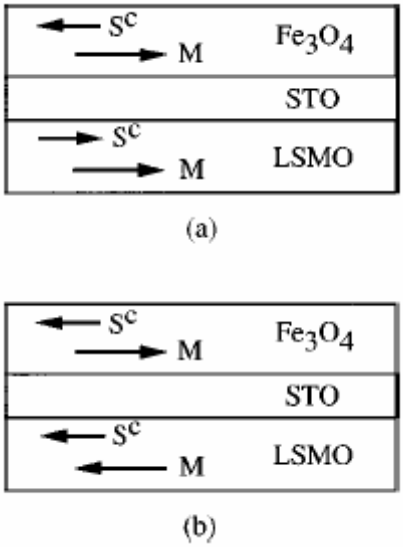

Fig. 2.6. Schematic showing two conditions of the magnetization and conduction electron spin orientations in the heterostructure corresponding to the (a) high and (b) low resistivity states [4].

In another work, Li *et al.* [6] prepared Fe_3O_4/MgO/ Fe_3O_4 MTJs on MgO substrates. In order to obtain different switching field (Fig. 2.7) for the top and bottom Fe_3O_4 layers, the bottom layer was deposited on $CoCrO_4$ buffer layer. At low temperature, the MH loop exhibited clear indication of two uncoupled magnetic layers. Figure 2.8 showed the magnetic field dependence of the tunneling resistance and the MR, $\Delta R/R_P$ (R_P was the peak resistance), at different temperatures. The switching fields for the increasing and decreasing resistance at various temperatures correspond closely to the magnetic coercivity of the top and bottom Fe_3O_4 layers (Fig. 2.7). A low resistance was observed at high fields, when the magnetization of the two layers is parallel. Besides, at field between the coercivities of the two layers, resistance reached the maximum value due to antiparallel orientation of the magnetization of two layers.

Although this study demonstrates the room temperature operation of Fe_3O_4 / MgO / Fe_3O_4 MTJs, the value of TMR is much smaller (~0.5% at 300K and ~1.5% at 150K) than expected. Several possibilities such as spin flip process due to the defective insulating barrier, formation of the magnetic dead layer at interface, or formation of antiferromagnetic oxides (e.g. Fe_2O_3) at the interface have been suggested.

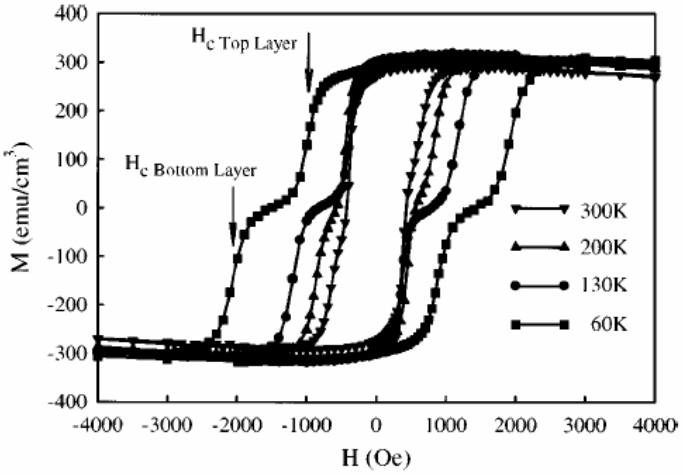

Fig. 2.7. Hysteresis loops at different temperature for Fe_3O_4/MgO/ Fe_3O_4 MTJ [6].

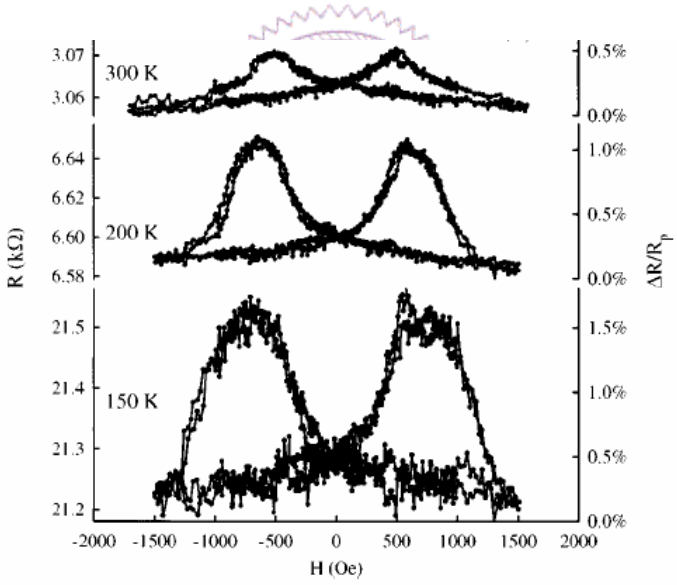

Fig. 2.8. Magnetotransport data for Fe_3O_4/MgO/ Fe_3O_4 MTJ at different temperature [6].

A noticeable large TMR was reported by Seneor et al. [5] in very thin Co/Al_2O_3/ Fe_3O_4 MTJs. A 15nm thick Co FM layer was deposited on glass substrate and followed by the deposition of 1.5 nm thick Al layer that was oxidized to form Al_2O_3. On top of Al_2O_3 layer, Fe_3O_4 layer of 1.5-2 nm was grown and capped with 15 nm Al layer. From the TEM analysis results, it indicated that there might exist a small fraction of γ-Fe_2O_3 phase in the Fe_3O_4 layer. At room temperature, these MTJs revealed TMR of about ~13%, which increased to as high 43% at 4.2 K (Fig. 2.9).

The interesting observation of this work is that the bias voltage dependence of conductance of these MTJs. The experiment results are shown in Fig. 2.10. The key feature is the abrupt drop of both the conductance and MR at very small bias voltage (±10 mV). A drop in the conductance was not observed for the NiFe/ Al_2O_3/Co tunnel junction (both curve in Fig. 2.10). This indicates the existence of a energy gap of about 10 mV for the tunneling behavior in the Co/ Al_2O_3/ Fe_3O_4 tunnel junction. The similar behavior for positive and negative bias but implies that this tunneling process is related to electronic level on both sides of the Fermi level.

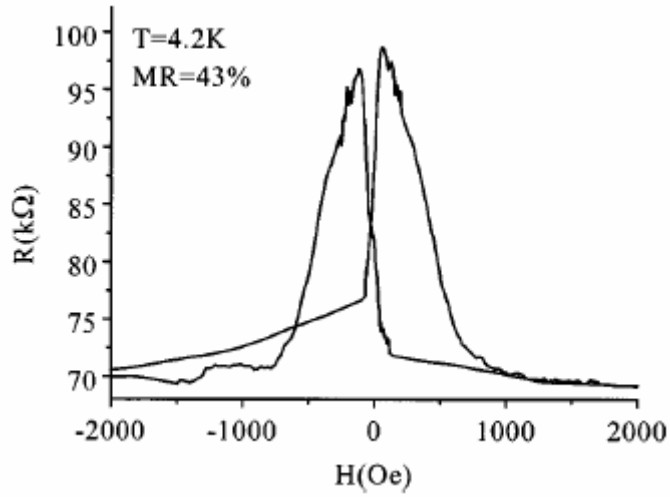

Fig. 2.9. TMR of $Co/Al_2O_3/ Fe_3O_4$ MTJ at 4.2K [5].

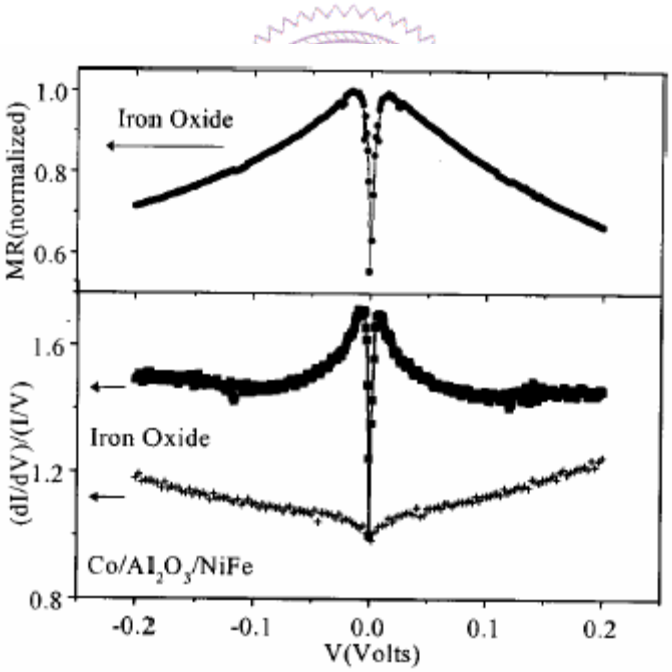

Fig. 2.10. Bias dependent MR and conductance of $Co/Al_2O_3/ Fe_3O_4$ MTJ. For comparison, the conduction data for $Co/Al_2O_3/ Fe_3O_4$ MTJ is also shown [5].

2.2 Dilute Magnetic Semiconductor – ZnCoO

2.2.a Properties of ZnO

ZnO is a wide band gap, optoelectronic material belonging to Ⅱ-Ⅵ family of semiconductor. It has a wurtitic hexagonal crystal structure, which Zn and O planes are alternately stacked along c-axis direction. The coordinations of Zn^{2+} and O^{2-} are both four-fold.

Table 2. II. describes structural, electrical, and optical properties of ZnO. ZnO has a direct energy band gap of 3.3 eV at room temperature. The energy band gap parameter, such as electron and hole effective mass, as well as optical and electrical properties are suitable for blue LED and semiconductor laser diode. On the other hand, ZnO is a much more intense and efficient UV emitter (at least 4 to 5 times more intense) at its band edge than GaN, due to that ZnO has a higher free excitation binding energy (60mV) that is more than twice than that of GaN (25mV). Based on these properties, that ZnO system was a good candidate for wide range of devices such as blue and UV light emitting diodes and spintronic device based on dilute magnetic semiconductor.

Basic properties		Crystal Lattice Properties	
Density *[g/cm^3]*	5.67	Crystal Structure	Wurtize
Molecular weight *[atomic unit]*	81.38	Lattice constant *[Å]*	a=3.24 c=5.20
Ion radius *[Å]*	r_{ZN}^{2+}=0.60	Stacking Fault energy *[mJ]*	100
Thermal Properties		**Electrical Properties**	
Melting point *[K]*	2242	Energy band gap *[eV]*	Eg = 3.27 (300K) Eg = 3.44 (6K)
Coefficient of Linear expansion *[10^{-6}/K]*	$\alpha_{//c}$=25.6 at 260K $\alpha_{\perp c}$=45.0 at 260K	Electron Hall mobility *[$cm^2/V \cdot s$]*	$\mu n_{\perp c}$ = 70 $\mu n_{//c}$ = 170
Thermal conductivity *[W/m · K]*	54		

TABLE 2. I.

Physical properties of ZnO [13].

2.2.b Theory of ZnO-based Dilute Magnetic Semiconductor

In this section, we focus on the ZnO-based type DMS [14]. The basic theory on understanding the magnetic properties of dilute magnetic semiconductors is mean-field theory.

A key development that focused attention on wide-band-gap semiconductors as being the most promising for achieving high Curie temperature was the work of Dietal et al [15]. By applying the mean-field theory based on the Zener ferromagnetism model [16], Dietl calculated the Curie temperature (T_C) for various semiconductors [15]. Based on the Zener model, the short bond length in wide-band-gap materials, such as ZnO, lead to a strong coupling between holes and spins when doped with transition metals. In addition, according to the mean-field approximation model, the T_C is determined by the competition between the ferromagnetic and anti-ferromagnetic interactions. Since the model also considers the anisotropy of the carrier-mediated exchange interaction related to the spin-orbital coupling in the host material, the T_C is proportional to the density of Mn ions and the hole density. The values of T_C computed for various semiconductors with 5% of Mn and 3.5×10^{20} holes/cm^3 are presented in Fig. 2.11. This model predicts the observation of a spontaneous magnetic moment at room temperature in transition-metal-doped nitrides and oxides [14].

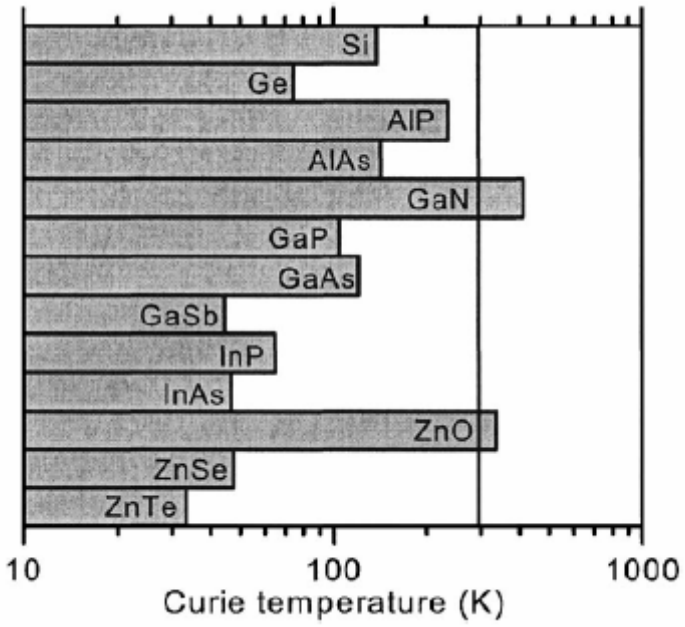

Fig. 2.11. Calculation results of the Curie temperature for various semiconductor. [15].

In addition to the prediction of Dietl, ferromagnetism in TM-ion-doped ZnO has been theoretically investigated by using *ab initio* calculations based on the local density approximation by Sato and Katayama-Yoshida [17-19]. The results suggest that ferromagnetic ordering of Mn is favored when mediated by holes. For Mn dopant, the transition from the antiferromagnetic state to the ferromagnetic state occurred as the holes were introduced, but no transition was found by n-type doping, as shown in the Fig. 2.12(a). However, for V, Cr, Fe, Co, and Ni dopants, ferromagnetic ordering in ZnO is predicted to exist without any additional charge carriers, as shown in the Fig. 2.12(b-d). According to the density of states, it was suggested that the ferromagnetism resulted from a competition between the ferromagnetic double exchange interaction and the anti-ferromagnetic super exchange

interaction. Figure 2.12 shows the transition from spin-glass state to FM state in ZnTMO (TM=Mn, Fe, Co, Ni) with acceptor doping for different TM concentrations. Unlike for the Mn dopant, the ferromagnetism becomes weaker for Fe-, Co-, and Ni- doped ZnO with increasing hole concentration. The stability of the ferromagnetic state for 3d transition-metal-doped ZnO with no additional carrier doping is shown in Fig. 2.13. It also revealed the ferromagnetic state was the ground state for V, Cr, Fe, Co, and Ni in ZnO. In conclusion, acceptor-doped (Zn,Mn)O and ZnO doped with other 3d transition metals were proposed as candidates of a ferromagnet.

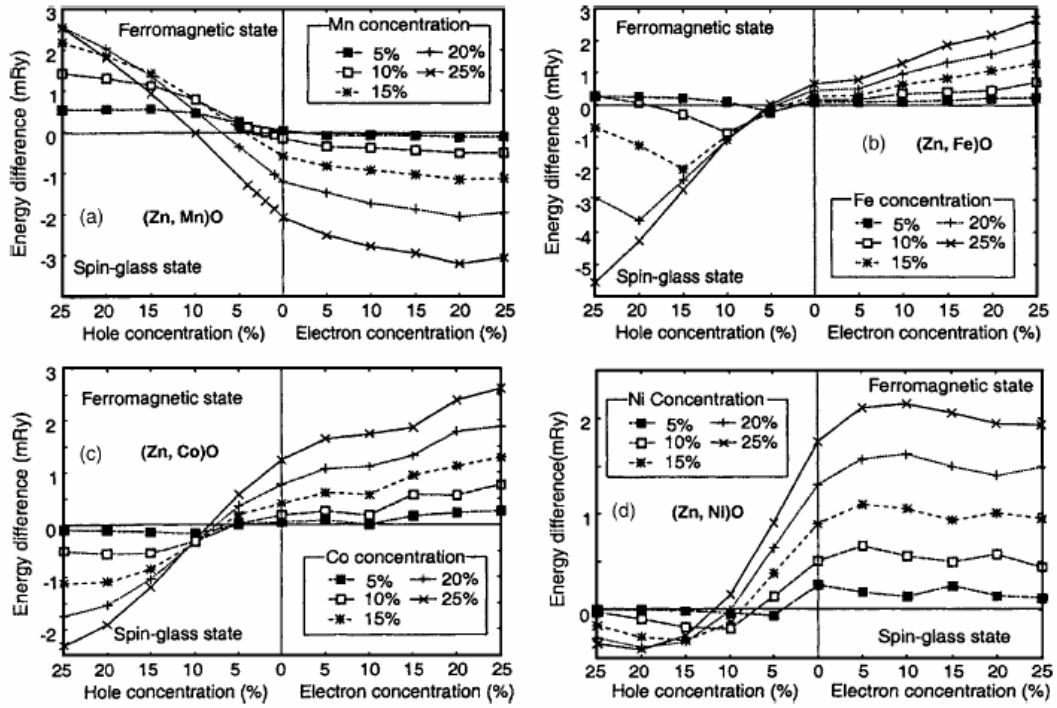

Fig. 2.12. Stability of the ferromagnetic state in (a)Mn-, (b)Fe-, (c)Co-, and (d)Ni-doped ZnO as a function of the carrier concentration. The vertical axis is the energy difference between the ferromagnetic and spin-glass state. A positive-energy difference indicates a more stable ferromagnetic state. [19].

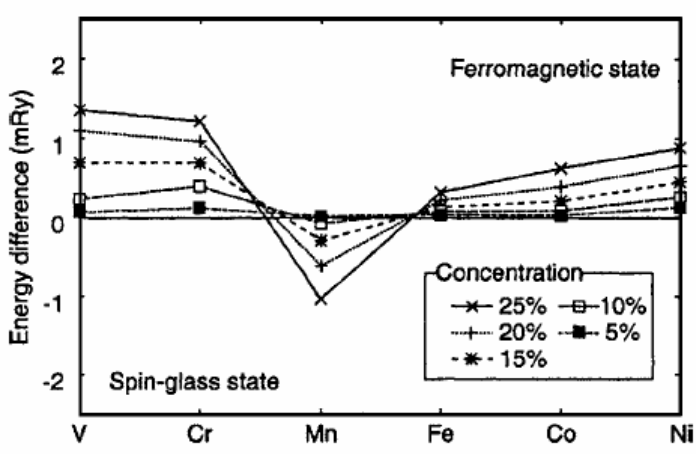

Fig. 2.13. Stability of the ferromagnetic state in V-, Cr-, Mn-, Fe-, Co-, and Ni-doped ZnO for different dopant concentrations. The vertical axis is the energy difference between the ferromagnetic and spin-glass state. A positive-energy difference indicates a more stable ferromagnetic state. [19].

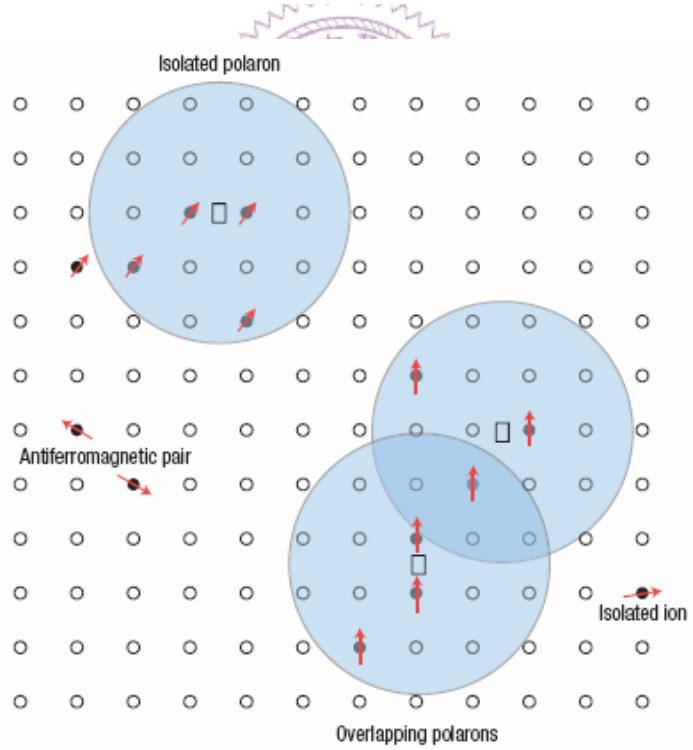

Fig. 2.14. Representation of magnetic polarons. Cation sites are represented by small circles. Oxygen is not shown; the unoccupied oxygen sites are represented by squares [19].

On the other hand, Coey et al. proposed the bound magnetic polaron (BMP) model which described that ferromagnetic ordering of the transition metal moment could originate from carrier that are existed in the material or localized at the transition metal ion. This model assumes an exchange interaction between the TM ion and part of localized charge carriers that are surrounded near the transition metal ions. When these BMP overlapped as shown in the Fig. 2.14, a long range ferromagnetic state could be obtained. Furthermore, Coey *et al*, also proposed the exchange interaction was mediated by shallow donor electrons that from BMP in n-type ZnTMO, which overlap to create a spin-split impurity band. Therefore, if there is sufficiently strong hybridization and charge transfer from the donors, the high Curie temperature could be expected. As shown in Fig. 2.15, Coey and coworkers have reported ferromagnetism in ZnO doped with Sc, Ti, V, Fe, Co, and Ni [20]. A large moment of 2.0 μ_B / Co was observed for the case of ZnCoO.

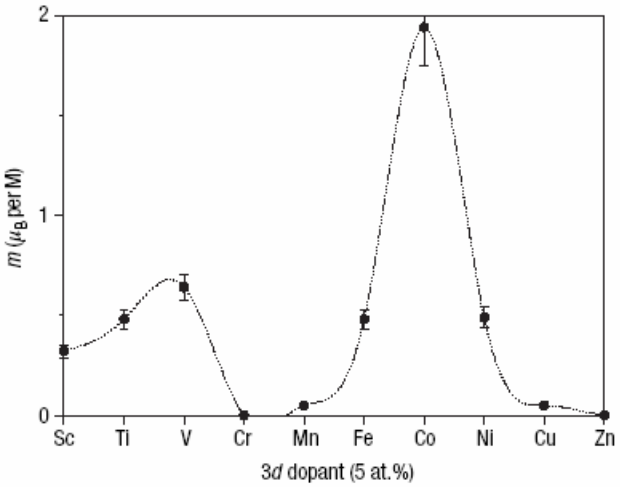

Fig. 2.15. The magnetic moment of thin films produced from $(Zn_{0.95}M_{0.05})O$ targets by pulse-laser deposition, for M = Sc to Cu, measured at room temperature [20].

2.2.c Experimental Results of ZnCoO-Based Dilute Magnetic Semiconductors

In this section, we introduce deposition methods, physical properties and identification approaches for ZnCoO thin films. In recent works, M.Kobayshi et at. [21] obtained an epitaxial $Zn_{1-x}Co_xO$ (x=0.05) thin film of 200nm was grown on an α-Al_2O_3 (0001) substrates by the pulsed laser deposition (PLD) system at 300℃. In their work, x-ray magnetic circular dichroism (XMCD) was performed to determine the electronic structure and magnetic properties associated with the Co ions. XMCD is the difference in absorption spectra between right-hand and left-hand side circular polarized x-ray. Since XMCD could probe the magnetic moment of a specific element, it would help us to identify the particular magnetic properties of substituted transition metal ions. XMCD signal of ZnCoO was shown in the Fig. 2.16. The difference between the XMCD spectra at H = 2 and 4.5 T, respectively, indicated the paramagnetic component of ZnCoO. Furthermore, we should notice that the XMCD spectra reveal the line shape and absorption edge position which were different to those of Co metal [22], indicated the doped transition metal ions are ferromagnetic in ZnO. In addition, the shape of Co L_2 edge is quiet similar to the tetrahedral multiplet spectra, indicated the consistent description of Co ions located at Zn site in tetrahedral coordination. In conclusion, the XMCD spectra show multiplet structures, characteristic of the Co^{2+} ion tetrahedrally coordinated by oxygen, suggesting that the ferromagnetism comes from Co ions substituting the Zn site in ZnO.

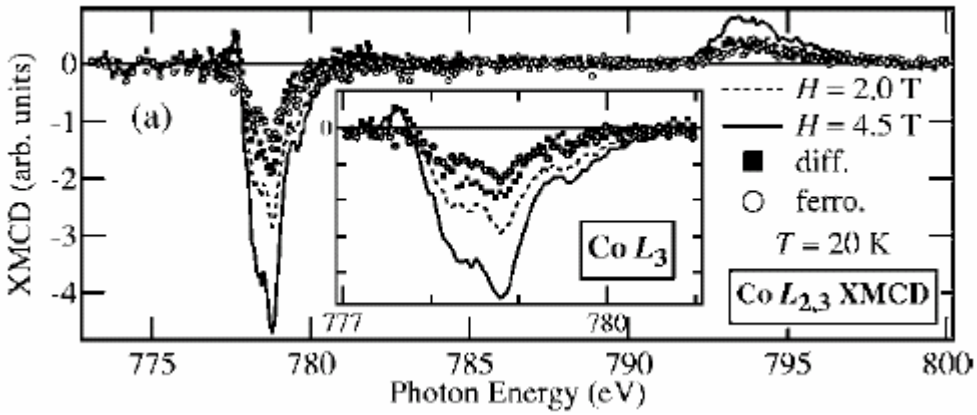

Fig. 2.16. XMCD spectra of ZnCoO under different magnetic field at 20K. Closed circle shows the difference of the spectra between H=4.5 and 2.0 T [19].

Another important evidence for intrinsic DMSs was the observation of the anomalous Hall effect (AHE) in thin films [23]. This criteria was also questioned because the AHE was also observed in the superparamagnetic Co-doped TiO_2 films [24]. However, AHE measurement is still a good tool to show the spin-orbital interaction in the material. In Peng's work [25], an epitaxial $Zn_{1-x}Co_xO$ (x=0.05) thin film was grown on an α-Al_2O_3 (0001) substrate by the dual pulsed laser deposition (DPLD) system. Two Hall voltage components were coexisted in the Hall measurement for a magnetic material [26]. The Hall resistivity ρ_B can be defined by

$$\rho_B = R_0 B \cos\alpha + R_A M \cos\theta$$

where R_0 is the ordinary Hall coefficient, B is the magnetic flux density, R_A is the anomalous Hall coefficient, M is the magnetization of the film,

α is the angle between the magnetization and the normal to the sample, and θ is the angle between the magnetization and normal to the sample. The first term in Eq. 2.XX is the ordinary Hall effect (OHE). The second term is the AHE and is due to spin-dependent scattering.

A small AHE signal of ZnCoO was observed as shown in the Fig. 2.17. Although the signal intensity was quiet small, it is evident that the AHE was really observed in the ZnCoO thin films. In their measurement conditions, the AHE signal was dominant at lower magnetic field and can be evaluated by subtracting the linear background. As we mentioned before, AHE measurement is strongly related to the *sp-d* interaction in the material. Therefore, the observation of AHE indicated that the ferromagnetic response of charge carrier in ferromagnetic semiconductor. It is a quiet important experimental evidence for carrier-mediated DMS.

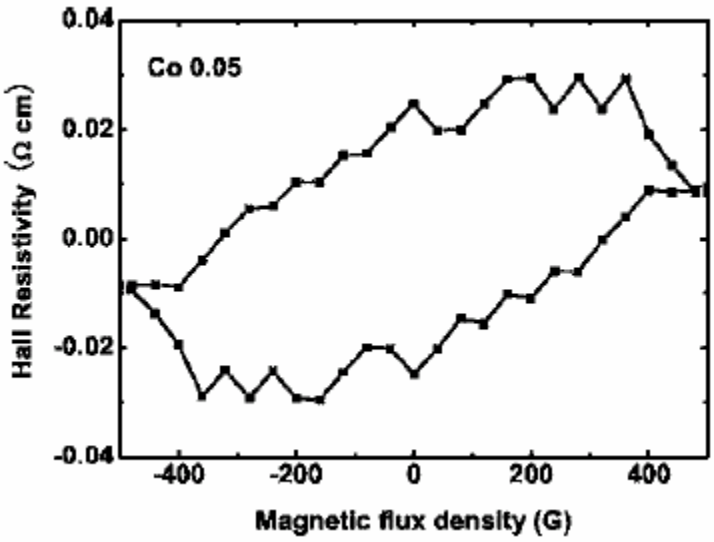

Fig. 2.17. AHE signal of ZnCoO thin film [25].

2.3. Tunnel Magnetoresistance (TMR)

TMR is a consequence of spin-dependent tunneling (SDT). The essence of SDT is an imbalance in the electric current carried by up- and down-spin electrons tunneling from a ferromagnet through a tunneling barrier. The origin of this phenomenon can be explained by the fact that the probability for an electron to tunnel through the barrier depends on its Fermi wave vector. In ferromagnetic metals, electronic bands are exchange split, which implies different Fermi wave vectors for the up- and down-spin electrons and consequently a tunneling probability depends on the spin. The SDT effect was discovered in pioneering experiments by Tedrow and Meservey [27]. Using superconducting layers as detectors they measured the spin polarization of the tunneling current originating from various magnetic electrodes across an alumina barrier, and which strongly supports the Tedrow and Meservey's model [27].

Although TMR has been known from the theory of Julliere [28] for almost 30 years, only a relatively modest number of studies had been performed in this field up to the mid-1990s. This was caused by the technologically demanding fabrication process, which makes it difficult to fabricate robust and reliable tunnel junctions. Also the face that the reported values of TMR were small (at beginning a few per cent at low temperatures) meant that no great interest was triggered as regards sensor/memory applications. However, Miyazaki and Tezuka [29] demonstrated the possibility of large values of MR ratio in TMR

junctions with Al_2O_3 insulating layers, and Moodera *et al*. [30] developed a fabrication process which appeared to fulfil the requirements for smooth and pinhole-free Al_2O_3 deposition. Since the first observation of reproducible, large MR ratio at RT, shown in Fig. 2.5, there has been enormous increase in the amount of research in this field. Nowadays TMR junctions that are based on 3d-metal ferromagnets and Al_2O_3 barriers can be routinely fabricated with MR ratios more that 70 % at room temperature, making them suitable for industrial applications [31-32] .

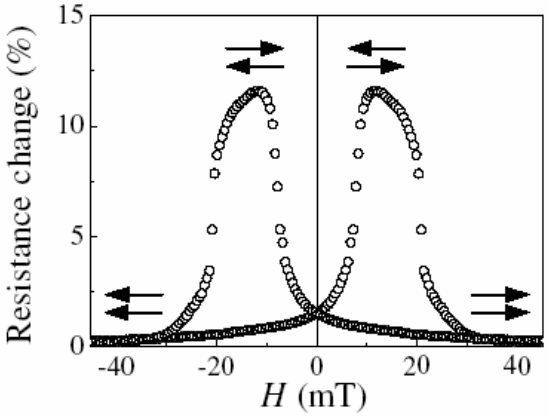

Fig. 2.18. The first observation of large room temperature MR ratio in a CoFe/Al_2O_3/Co TMR junction. The arrows indicate the relative magnetization orientation in CoFe and Co layers [25].

In the following sections, we will address various factors that control the magnitude of magnetoresistance in TMR junctions. Starting from early experiments on spin-dependent tunneling and their interpretation, we consider then several theoretical models, which highlight the role of the electronic structure of the ferromagnets, the insulating layer, and the ferromagnet/insulator interface.

2.3.a Experiments on Spin-Dependent Tunneling

The field of spin-dependent tunneling (SDT) was founded by the pioneering experiments of Tedrow and Meservey [27]. They used ferromagnet/insulator/superconductor (FM/I/S) tunnel junctions to measure the spin polarization of the tunneling current originating from various ferromagnetic metals across an alumina insulating barrier. In these experiments, electrons tunnel through the barrier to a superconducting Al film which acts as a spin detector. The superconducting DOS has a gap of 2Δ in the quasiparticle spectrum and characteristic singularities at $E=\pm\Delta$. If the thin superconducting film is placed in a magnetic field $\boldsymbol{H}$ applied parallel to the film plane, the quasiparticle states in the superconductor are split due to the Zeeman interaction of the magnetic field with the electron split magnetic moment. In this case, the DOS of the superconductor is the superposition of the up- and down-spin contributions separated by energy of $2\mu_B H$, as shown in Fig. 2.19(a). The orientation of the magnetic moment and therefore the spin directions are defined by the applied field.

The sharply peaked DOS of the superconductor makes it possible to separate the contributions from the up- and down-spin electrons in the tunneling current. As a result, tunneling from a ferromagnetic metal into such a superconductor gives rise to an asymmetric conductance curve, which is schematically shown in Fig. 2.19(b). This asymmetry is the consequence of the fact that electronic states in the ferromagnetic metal

are exchange split, which leads to an unequal DOS in the ferromagnet at the Fermi energy, $\rho^{\uparrow} = \rho^{\downarrow}$. Since $\rho^{\uparrow}$and $\rho^{\downarrow}$ determine the number of electrons which can tunnel within each spin channel, the spin conductance is weighed with the respective spin DOS. Assuming that spin does not change in the tunneling process, i.e. the total conductance is the sum over the up- and down-spin channels, $G = G^{\uparrow} + G^{\downarrow}$, the tunneling spin polarization can be obtained by measuring the relative heights of the conductance peaks displayed in Fig. 2.19, as written in equation 2.1.

$$P = \frac{G^{\uparrow} - G^{\downarrow}}{G^{\uparrow} + G^{\downarrow}} = \frac{(\sigma_4 - \sigma_2) - (\sigma_1 - \sigma_3)}{(\sigma_4 - \sigma_2) + (\sigma_1 - \sigma_3)} \qquad \text{(equation 2.1)}$$

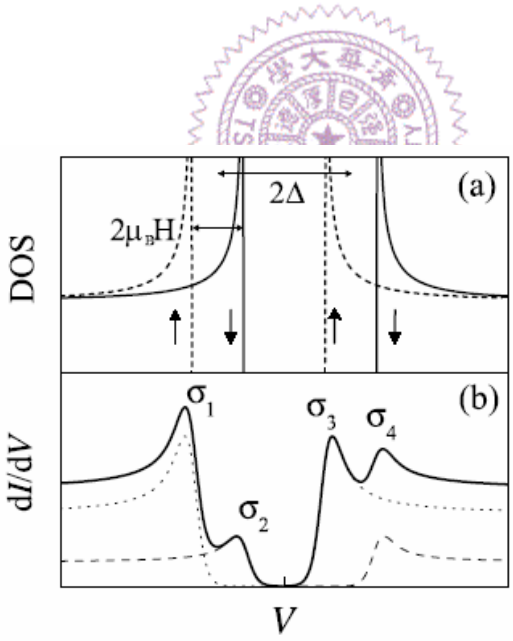

Fig. 2.19. Tunneling in a ferromagnet/insulator/superconductor junction. (a) The DOS of the superconductor split by a value of $2\mu_B H$ into the up- and down-spin contributions. (b) Conductance as a function of voltage for each spin orientation and the total conductance (solid curve)[28].

A more accurate determination of the tunneling spin polarization in

FM/I/S junctions must account for spin–orbit scattering in the superconductor [33]. Table 2.Ⅱ shows the experimental values of the spin polarization of the tunneling current across Al_2O_3 into superconducting Al from various ferromagnetic 3d metals corrected for the spin–orbit scattering. Along with the values of *P* obtained in early experiments [33], recently measured values are shown in Table 2.Ⅱ These new values of the spin polarization are higher than the old ones due to improved deposition techniques resulting in cleaner junctions with better interfaces.

TABLE 2.Ⅱ.

Spin polarization obtained in experiments on FM/Al_2O_3/Al tunnel junctions.

FM	Ni	Co	Fe	$Ni_{80}Fe_{20}$	$Ni_{40}Fe_{60}$	$Co_{50}Fe_{50}$	$Co_{84}Fe_{16}$
P(%),[28]	23	35	40	32	-	-	-
P(%),[34,35]	33	42	45	48	55	55	55

The results of these early experiments on SDT were interpreted in terms of the DOS of the ferromagnetic electrodes at the Fermi energy. Assuming that the spin conductance is proportional to $\rho^{\uparrow}$ for the majority-spin electrons and is proportional to $\rho^{\downarrow}$ for the minority-spin electrons, we arrive at the result that the measured values of the spin polarization of the tunneling conductance, *P*, should be equal to the spin polarization of the DOS at the Fermi energy of the ferromagnet:

$$P_{FM} = \frac{\rho^{\uparrow} - \rho^{\downarrow}}{\rho^{\uparrow} + \rho^{\downarrow}} \qquad \text{(equation 2.2)}$$

2.3.b Tunnel Magnetoresistance Model – Julliere's Model

An important advance was made by Julliere [28] in 1975, a few years later after the successful experiments on SDT were reported. In these experiments the superconducting film was replaced by another ferromagnetic metal film, thereby making a FM/I/FM tunnel junction. It was reported that instead of using magnetic-field-induced spin-split states of a superconductor as a spin detector it is possible to use exchange-split states of another ferromagnet. In this case, it was expected that the tunneling current should depend on the relative magnetization orientation of the two ferromagnetic electrodes, giving rise to MR ratio. This is in fact what was observed. Using Co and Fe ferromagnetic films with different coercivity and a Ge barrier layer, Julliere observed sizable magnetoresistance at 4.2 K. The maximum MR ratio was found to be about 14% at zero bias, but decreased very rapidly with increasing bias voltage. This rapid decrease in TMR was attributed to spin-flip scattering at ferromagnet/barrier interfaces.

Julliere interpreted these results in terms of a simple model, which is based on two assumptions. First, he assumed that spin of electrons is conserved in the tunneling process. It follows, then, that tunnelings of up- and down-spin electrons are two independent processes, so the conductance occurs in the two independent spin channels. Such a two-current model is also used to interpret the closely related phenomenon of GMR. According to this assumption, electrons

originating from one spin state of the first ferromagnetic film are accepted by unfilled states of the same spin of the second film. If the two ferromagnetic films are magnetized parallel, the minority spins tunnel to the minority states and the majority spins tunnel to the majority states. If, however, the two films are magnetized antiparallel the identity of the majority- and minority-spin electrons is reversed, so the majority spins of the first film tunnel to the minority states in the second film and vice versa. Second, Julliere assumed that the conductance for a particular spin orientation is proportional to the product of the effective DOS of the two ferromagnetic electrodes. According to these assumptions, the conductance for the parallel and antiparallel alignment, G_P and G_{AP}, can be written as follows:

$$G_P \propto \rho_1^{\uparrow}\rho_2^{\uparrow} + \rho_1^{\downarrow}\rho_2^{\downarrow} \quad ; \quad G_{AP} \propto \rho_1^{\uparrow}\rho_2^{\downarrow} + \rho_1^{\downarrow}\rho_2^{\uparrow}, \qquad \text{(equation 2.3)}$$

where $\rho_i^{\uparrow}$ and $\rho_i^{\downarrow}$ are the tunneling DOS of the ferromagnetic electrodes (designated by index i = 1, 2) for the majority- and minority-spin electrons. It follows from equations (2.3) that the parallel- and antiparallel-magnetized TMR junctions have different conductances, which implies a non-zero MR ratio. We define TMR as the conductance difference between parallel and antiparallel magnetizations, normalized by the antiparallel conductance, i.e.

$$TMR \equiv \frac{G_P - G_{AP}}{G_{AP}} = \frac{R_{AP} - R_P}{R_P} \qquad \text{(equation 2.4)}$$

Using equation (2.3), we arrive then at Julliere's formula:

$$TMR = \frac{2P_1P_2}{1 - P_1P_2}$$ (equation 2.5)

where P is the spin polarization of ferromagnetic layer, as defined in equation (2.1).

The Julliere's model stimulated further research in the field of TMR junctions. However, the model is too simple to take the barrier quality into account. Nevertheless, the importance of the paper by Julliere should not be underestimated—in particular, his simple quantitative model which was later used by many researchers to correlate the magnitude of TMR ratio in TMR junctions with the spin polariztion of ferromagnets measured in experiments on FM/I/S tunnel junctions.

2.3.c MgO-based Magnetic Tunnel Junctions [14]

In the past few years, some theoretical calculations have predicted very high MR in epitaxial MTJs structures when the momentum of conduction electrons is conserved during the tunneling process, such as in (001) oriented Fe/MgO/Fe stacks [36,37]. At the Fermi energy of Fe in the (001) directions, only a state of Δ_1 symmetry was applied for the majority spins, but not for the minority. On the other hand, the states of Δ_1 symmetry decay much more slowly in the MgO barrier and the Δ_1 symmetry states can not propagate in the minority channel. Therefore, the

tunneling conductance of Fe/MgO/Fe stack is dominated by the majority channel for the parallel in Fe. In conclusion, an extremely high MR ratio is expected for the coherent spin-polarized tunneling. According to the theoretical calculation, the MR is expected to enhance with the increasing MgO thickness, and reach a maximum value above 1000% for about 10 atomic planes of MgO [14].

Due to the theoretical prediction by Bulter *et al*, fully epitaxial Fe(001) / MgO(001) / Fe(001) MTJ structures have been investigated by global research groups [38]. Since the TMR can be extremely large in such structures, it is expected to be limited by any disorder that may be present at the barrier interface. By the process optimization and better control of the interface, a MR ratio as high as 88% has been observed at room temperature (146% at 20K) in epitaxial stacks with MgO barrier grown by MBE as shown in Fig. 2.20 [39].

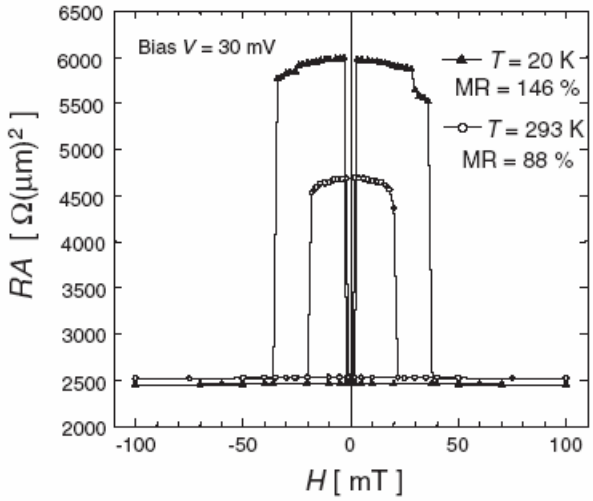

Fig. 2.20. Magnetoresistance curves for Fe(001) /MgO(001)/Fe(001) MTJ at T = 293 and 20 K. The MR ratios were 88% and 146%, respectively [39].

The bias dependence for MgO-based junctions is smaller than in tunnel junctions with AlOx barrier and reveal an asymmetric behavior. The bias voltage where the MR ratio reaches half of the zero-bias value were 1250 and 350 mV for the positive and negative bias directions, respectively. We should emphasize that the value for the positive bias direction is much higher than observed for AlO_X junctions. Parkin *et al.* reported that sputtered-deposited MTJs grown on amorphous underlayer, but with highly oriented (001) MgO tunnel barrier and CoFe electrodes, reveal MR values of up to ~ 220% at room temperature and ~300% at low temperature [40]. These textured MTJ stacks which were grown by standard sputtering process reveal more conventional capability, as compared to fully epitaxial structure which were grown by MBE. Besides, these MTJs exhibit higher MR at annealing temperature up to 400℃ result from the improvement of the MgO crystalline quality, as shown in the Fig. 2.21.

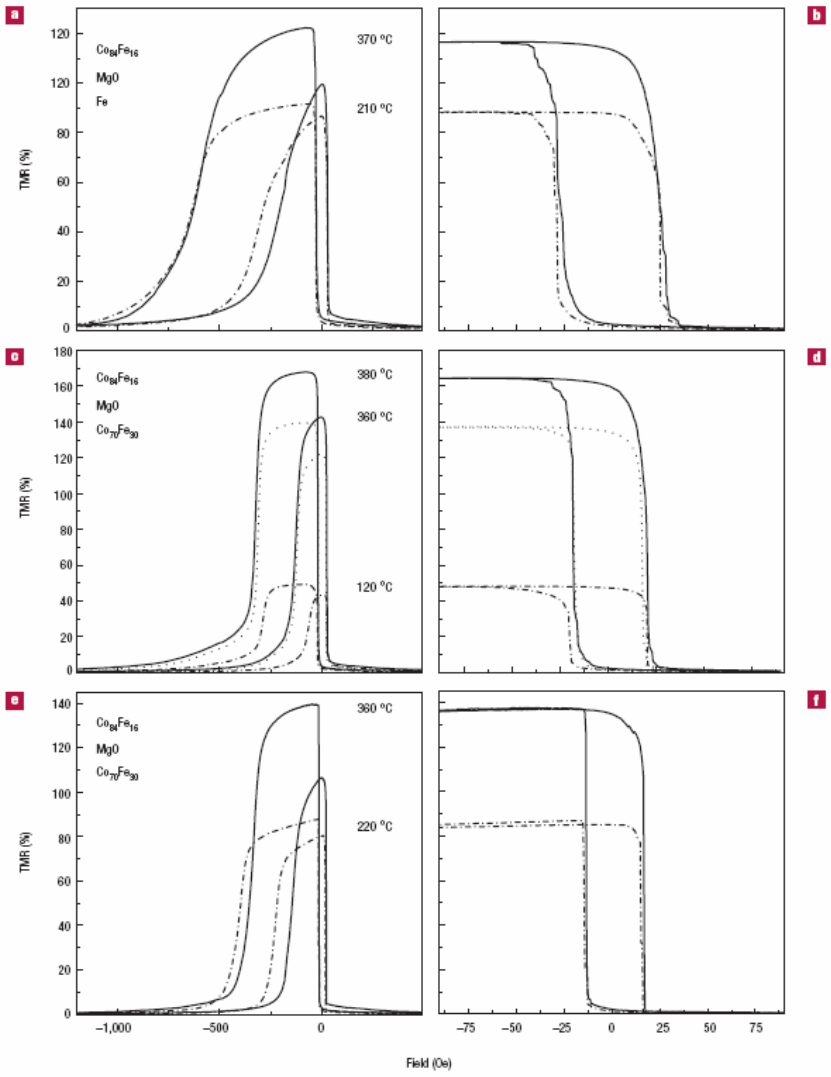

Fig. 2.21. Major and minor loops for MgO barrier with various electrode combinations. The experiment results show very high MR for all cases which increases further upon annealing at high temperature [40].

2.4 Exchange Bias Coupling

2.4.a Exchange Anisotropy

Exchange anisotropy was first discovered in partially oxidized Co particles by Meiklejohn and Bean [36]. Their discovery was initiated by the observation that the hysteresis loop below room temperature of nominal Co nano-particles was shifted along the field axis after cooling in an applied field. It was subsequently established that the particles had been partially oxidized to CoO, which is an antiferromagnet. Thus, the particles could be considered to consist of a core of single-domain Co with a shell of antiferromagnetic CoO. A compact of these particles was then cooled in a magnetic field to 77K, and its hysteresis loop was measured at that temperature. The hysteresis loop, as shown in Fig. 2.20(a), is not symmetrical about the origin but is shifted to one side. The shift of the center of the hysteresis loop from the origin is defined as the magnitude of the exchange field H_e. In addition, Co-CoO particles displayed unidirectional, rather than uniaxial, anisotropy [42]; therefore, the torque curves of those samples have a sin θ component as shown in Fig. 2.20(b). The field-cooled samples have another unusual characteristic: the rotational hysteresis loss W_r, which is defined as the area between counterclockwise and clockwise curves of the torque measurement, measured at 77K, remains high even at a high field. It is noteworthy that the above effects are not present (or are reduced) if the system is cooled in zero field from a demagnetized state. However,

exchange bias properties are still present if the system is zero-field cooled from a remanent state [43].

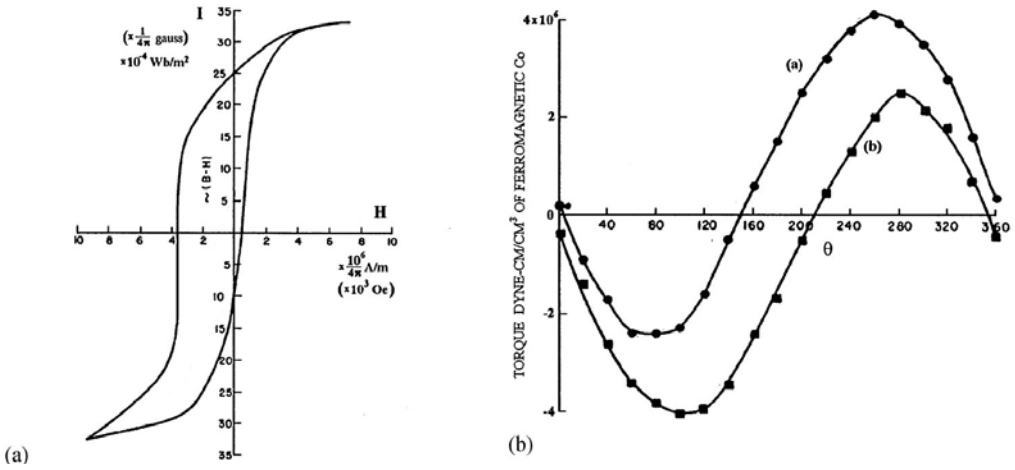

Fig.2.22. (a) The hysteresis loop, and (b) the torque curves for the Co-CoO sample cooled in the field and measured at 77K. Curve a and b in (b) are for countercloclwise and clockwise rotations, respectively. The area between curve a and b is the rotational hysteresis loss. (Data are from Meiklejohn's study of Co/CoO [42].)

Since the first experiments of Meiklejohn and Bean, many FM/AFM systems have been explored to increase the scientific understanding of them. Exchange anisotropy was not of interest to industry until Hempstead *et al.* [44] proposed that unidirectional exchange anisotropy between NiFe and FeMn could be useful for biasing small magnetoresistive sensors and also for suppressing Barkhausen noise. However, it was the reduction of the saturation fields to obtain giant magnetoresistance (GMR) in exchange biased systems [45], as compared to standard GMR multilayer systems [46], which triggered a renewed interest in these phenomena [47].

In addition to the symmetry breaking related to the appearance of the unidirectional anisotropy that brings about the exchange field, several supplementary remarkable features are associated with exchange anisotropy. One of them is the existence of a critical temperature called blocking temperature, T_B, above which exchange anisotropy vanishes. Usually T_B can be considerably lower than the Néel temperature of coupled ferromagnet. Another remarkable feature of exchange anisotropy is the training effect, i.e. the dependence of exchange field on the number of measurements n, with the value of H_e decreasing as n increases [48], which constitutes a hint that the interface actually is in metastable equilibrium. More recently, an important additional feature was discovered: the memory effect, which consists of the fact that the system keeps a memory of the temperature at which it was field-cooled [49]. Still, another characteristic associated with many exchange anisotropy systems, observed at $T < T_B$, is a large increase of the coercivity. The effect of the cooling field amplitude or the effect of the field applied during growth is rarely reported. This is probably because H_e does not depend markedly on cooling field [43]. However, studies in Fe/FeF_2 and Fe/MnF_2 bilayers revealed a rather unusual behavior [50]. The most striking result is that for large cooling fields the loops instead of shifting towards negative field, they shift to positive field. This is contrary to what is observed for small cooling field or what is observed in other systems. This effect is often called positive exchange bias.

Several models for the exchange anisotropy have been proposed. However, no one can successfully explain all the experimental findings. It is believed that the exchange anisotropy strongly depends on the spin structure at the interface, which is difficult to detect by using conventional methods. Both intrinsic properties, such as spin orientation or anisotropy, and extrinsic properties, e.g. roughness or crystallinity, contribute to exchange anisotropy. Consequently, the exchange anisotropy is a combination of many factors, which makes its theoretical analysis complicated. Several models for the exchange anisotropy of the F/AF system are introduced as following.

2.4.b Ideal Interface Model

The first simple model for exchange anisotropy was built by Meiklejohn and Bean [42]. They examined the exchange coupling across an ideal interface as shown in Fig. 2.23. The FM and AFM are both single crystalline and epitaxial across an atomically smooth interface. In this model, the switching field of the FM coupled to the AFM is determined by balancing the Zeeman, magnetocrystalline anisotropy, and exchange anisotropy energies. By assuming that the external field is not large enough to affect the sublattice magnetization of AFM, and the dominant anisotropy energy in FM and AFM is uniaxial magnetocrystalline anisotropy and their easy axes are aligned with each other, the general formula of total energy per unit area E (erg/cm^2) in this system can be expressed as:

$$E = -H M_s t_F \cos(\theta-\theta_F) + K_F t_F \sin^2\theta_F - K_e \cos\theta_F \qquad \text{(equation 2.6)}$$

where the $M_s, t_F, K_F, K_e, \theta$, and θ_F represent the saturation magnetization of the FM, the thickness of the FM, the uniaxial anisotropy constant of the FM, the interfacial coupling constant, the angle between applied field and easy axis, and the angle between magnetization of FM and easy axis, respectively.

The energy consists of the following three energies: (1) the Zeeman energy, $H M_s t_F \cos(\theta-\theta_f)$, (2) the magnetocrystalline anisotropy of the FM, $K_F t_F \sin^2\theta_F$, and (3) the exchange anisotropy energy, $-K_e \cos\theta_F$.

This model for exchange anisotropy is straightforward and describes the observed shifted hysteresis loop and $\sin\theta$ torque curve. However, the exchange field estimated by the model is two-to-three orders larger than the experimental value of the exchange field in the NiFe/FeMn system [46]. It is interesting to point out that, if one adopts this ideal model as a guide for an intuitive picture, one is to expect: (1) the uncompensated interfaces should exhibit the largest magnitudes of H_e; and (2) the roughness of a compensated interface should increase the magnitudes of H_e. However, the experimental results [38] show that none of these expectations is fulfilled.

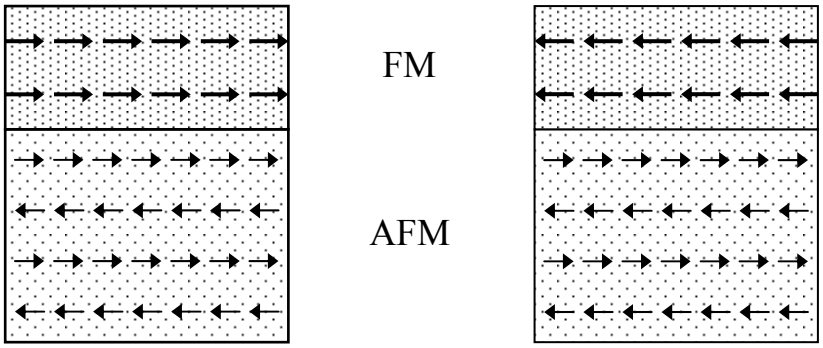

Fig. 2.23. Schematic diagrams of spin configurations of the ideal FM/AFM interface.

2.4.c Random Field Model

Malozemoff rejects the assumption of an atomically perfect uncompensated boundary exchange. He proposed a random-field model [51], in which an interfacial AFM moment imbalance originates from features such as roughness and structural defects. Consider a rough interface, starting with a single monoatomic bump in the compensated simple cubic interface, as shown in Fig. 2.24. In these two configurations, the orientation of the spins in AFM is the same, but in FM the spins oppose each other. The local bump introduces more antiparallel pairs, marked as crosses, in configuration (a) than in configuration (b). Consequently, the local roughness leads to a difference of local interfacial energy $\Delta\sigma_l = zJ/a^2$, where z is the number of order unity, i.e., the correlation number related to the number of antiparallel pairs, J is the interfacial exchange coupling constant, and a is the atomic spacing. This model argues that a net average non-zero

interfacial energy will exist, particularly when the average is taken over a small number of sites. Statistically, the average $\Delta\sigma$ in an area of L^2 will decrease as $\Delta\sigma \approx (\Delta\sigma_l/\sqrt{N})$ where $N = (L^2/a^2)$ is the number of sites projected onto the interface plane. Given the random field and assuming a single domain FM film, the AFM film will divide into domain-like regions normal to the interface to minimize the net random unidirectional anisotropy.

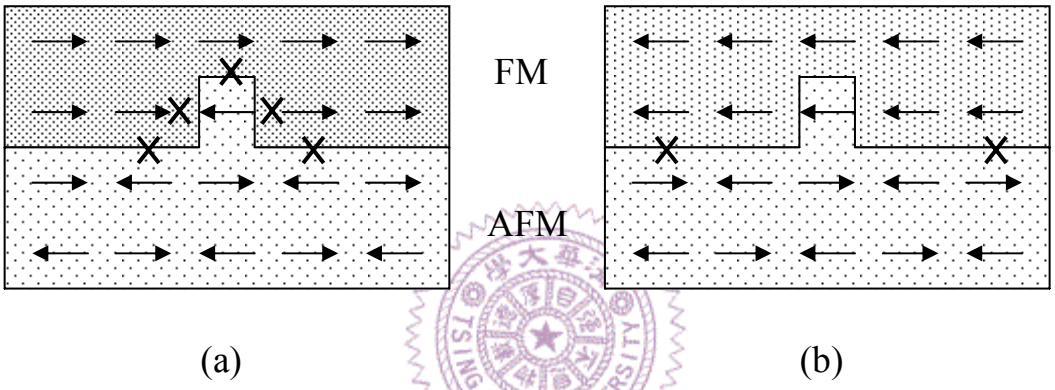

Fig. 2.22. Schematic diagrams of possible spin configurations in the random field model.

Although expansion of the domain size L would lower the random field energy, in-plane uniaxial anisotropy energy K_{AF} in the AFM layer will limit the domain size. Anisotropy energy confines the domain wall width to $\pi\sqrt{A_{AF}/K_{AF}}$, and creates an additional surface energy term of the domain wall $4\sqrt{A_{AF}K_{AF}}$ (surface tension in bubble domain), where the $A_{AF} \approx$ J/a is the exchange stiffness in AFM and K_{AF} is the anisotropy constant of the AFM. The balance between exchange and anisotropy energy is attained when $L \approx \pi\sqrt{A_{AF}/K_{AF}}$. Therefore, the average

interfacial exchange energy density becomes

$$\Delta\sigma = \frac{4zJ}{\pi aL} \qquad \text{(equation 2.4)}$$

Accordingly, the exchange field due to the interfacial random-field energy density is

$$H_e = \frac{\Delta\sigma}{2\,M_F\,t_F} = \frac{2z\sqrt{A_{AF}K_{AF}}}{\pi^2 M_F\,t_F} \qquad \text{(equation 2.5)}$$

The factor of $\sqrt{A_{AF}K_{AF}}$ reduces the predicted exchange field to the levels observed in experiments of the NiFe/FeMn system. However, the most debatable point in this model is the estimation of the AFM domain size. If the size of the AFM domains is on the same order as that of the domain walls, this implies that most of the interface area actually consists of domain walls! It is not clear from this model how the exchange field is affected by the AFM domain walls at the interface.

2.4.c AFM Domain Wall Model

To explain the discrepancy between the exchange field value predicted by Equation (2.2) and experimental observations, Mauri *et al.* [52] proposed an alternative model shortly after Malozemoff's proposal. They proposed the formation of a planar domain wall at the interface with the reversal of the FM orientation. Assuming that the thickness of FM,

t_F, is much smaller than the FM domain wall width, the domain wall will develop inside the AFM, as shown in Fig.2.25.

The energy required per unit area of this domain wall is $2\sqrt{A_{AF}K_{AF}}$. The FM reverses when the Zeeman energy of the ferromagnet is greater than the energy required to form a domain wall in the AFM. This leads to the more realistic equation $H_e M_s t_F = 2\sqrt{A_{AF}K_{AF}}$. Therefore, the model predicts that the exchange field is given by

$$H_e = \frac{2\sqrt{A_{AF}K_{AF}}}{M_F t_F} \qquad \text{(equation 2.9)}$$

In this model, the exchange energy is not concentrated across a single atomic interface but spreads out over a domain wall of width $\sim\sqrt{A_{AF}K_{AF}}$. This leads to a reduction of H_e by a factor of $\sqrt{A_{AF}K_{AF}}$, the same reduction arrived at as with the random field model. However, the AFM domain wall model fails to explain the persistence of exchange anisotropy without diminution of H_e, down to an AFM thickness of 25Å, an order of magnitude lower than the characteristic domain wall width.

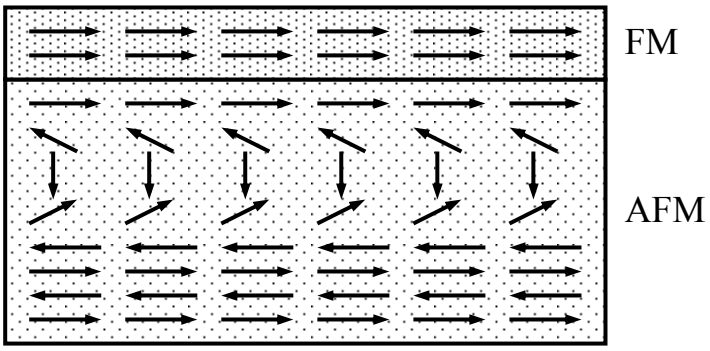

Fig. 2.25. Schematic diagram of spin configurations in the AFM domain wall model.

2.4.d Interfacial Spin Model

Takano *et al.* studied the CoO/ MgO multilayers and NiFe / CoO bilayers to clarify the importance of uncompensated spins of AFM layer at the interface in exchange anisotropy [53]. CoO/MgO multilayers were used to determine the magnetic properties of uncoupled CoO films since MgO is nonmagnetic. The multilayers were cooled from 350 to 10 K in zero field (ZFC) and in +10 kOe (FC) and their thermoremanet moments (TRM) were measured. Fig. 2.26 (a) shows the FC and ZFC measurements for the [CoO (10.3 nm)/ MgO (3nm)]$_{15}$ multilayers. The interfacial TMR density exhibits two feature (1) an intermediate temperature region (200 > T > 50 K), where the magnetization is independent of temperature and (2) a low temperature increase (T < 50 K). The magnitudes of these two features scale closely with the number of CoO layers and have no dependence on the net CoO thickness in the multilayers. Therefore, the uncompensated moment of both features is an interface effect but not a bulk effect. From the neutron data, the measured interfacial uncompensated moment represents ~ 1% of the spins in a CoO monolayer. The NiFe / CoO bilayers were cooled from 350 to 10 K in a +10 kOe. Figure 2.27 shows $H_E(T)$ of the bilayers with various CoO thickness. $H_E(T)$ of the NiFe / CoO films exhibit the plateau and low temperature increase features in the identical temperature regions, similar to the TRM of the Co. If the TRM of the CoO (10.3 nm)/ MgO (3nm) multilayers and $H_E(T)$ of the NiFe / CoO (10 nm) bilayer are normalized at 70 K, the curves overlap at all temperatures. This correlation strongly

suggests that the interfacial uncompensated AFM spins is consistent with measured NiFe / CoO exchange field ~ 1% derived from ideal interface model [53]. In addition, the H_E dependent with CoO thickness suggests a structure origin for the density of uncompensated spins. The exchange bias in the systems exhibits inverse proportional to the CoO crystallite diameter resulting from the different growth thickness. From the theoretical calculations, Takano *et al.* proposed that the surface morphology including roughness and grain size strongly affect the amount of uncompensated spins at the interface and, thus, exchange bias in the FM / AFM bilayers.

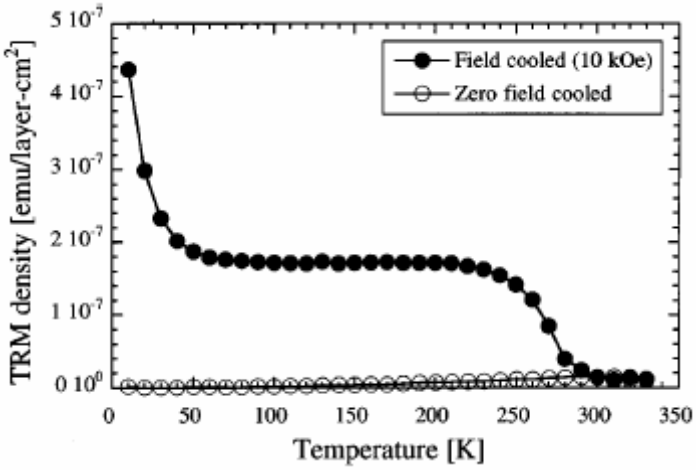

Fig. 2.26. FC and ZFC moment densities vs temperature of the [CoO (10.3 nm) / MgO (3 nm)]$_{15}$ multilayer [48].

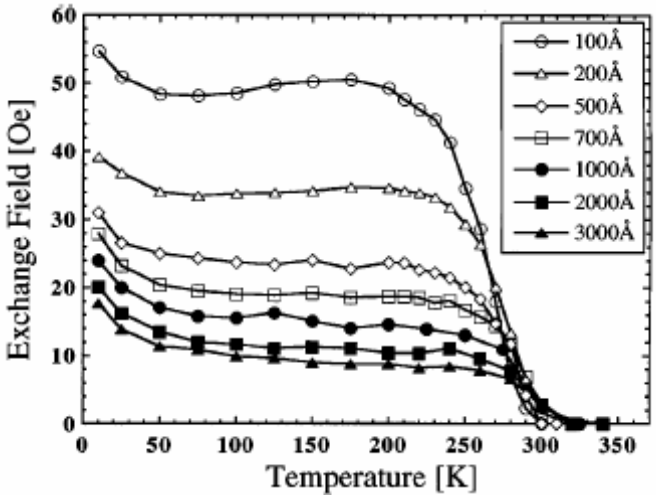

Fig. 2.27. Temperature dependence of H_E for permalloy (30 nm) / CoO bilayers with CoO thickness of 10 to 300 nm [48].

However, the existence of uncompensated interfacial spins is insufficient for inducing exchange bias since it may rotate together with the ferromagnetic layer, leading to no exchange bias. Ohldag et al. [54] prepared the exchange bias sample of IrMn/Co. They used high sensitivity XMCD spectroscopy to identify uncompensated Mn spins, located at AFM-FM interface.

In Fig. 2.28, the XMCD signal obtained from Co and Mn in the field growth (left) and zero-field growth (right) Co/IrMn along the parallel and antiparallel (address in the figure) to the propagation direction of the incident x rays. The Co spins in the FM and Mn spins in the AFM both revealed identical H_C, bias field and similar shape. Besides, the Mn signal of the field growth sample exhibited a small vertical shift that was absent in the Mn loops of zero-field growth sample. The vertical shift in

the Mn loops, indicated that only a small fraction of the total uncompensated moments is pinned in the exchange biased sample. According to the experiment results, only about 4% of the interfacial spins is highly pinned to AFM and does not rotate in an applied magnetic field. Since only those pinned interfacial spins would contribute to the exchange bias field, the exchange field ~ 4% derived from ideal interface model [53]. Obviously, the vertical magnetization shift played an important role in investigating the exchange bias behavior. However, it is difficult to directly observe the vertical magnetization shift with conventional measured FM/AFM hysteresis loops.

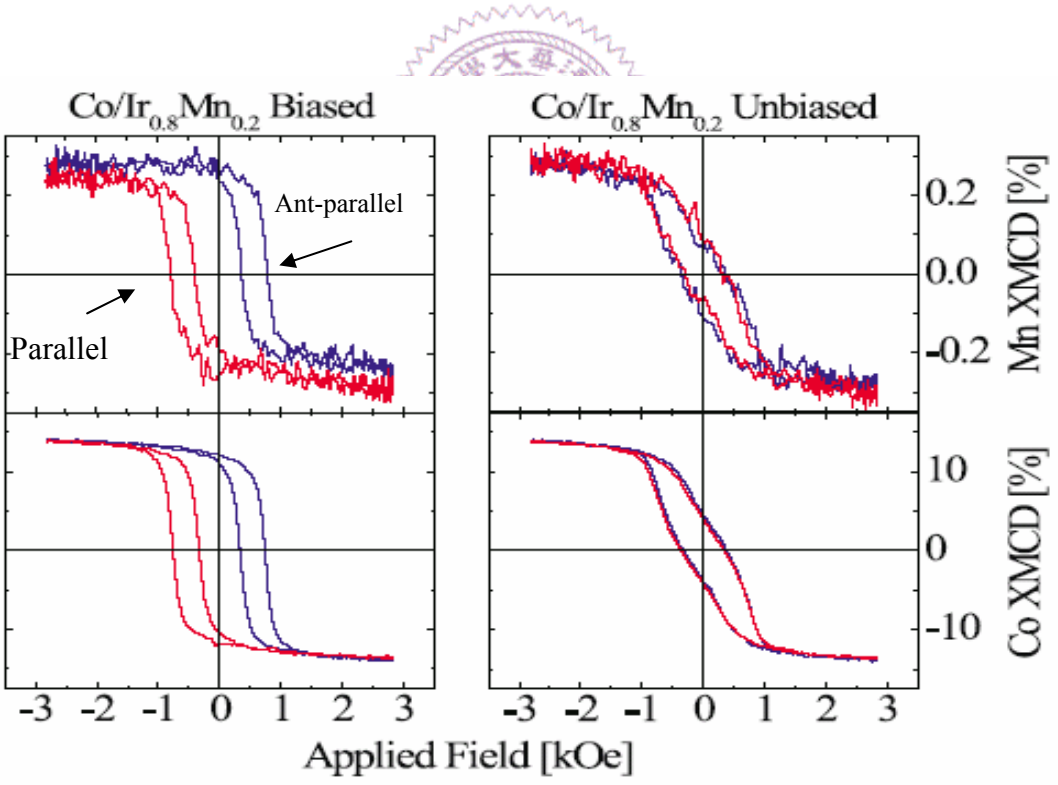

Fig. 2.28. Element specific XMCD loops measured on Co and Mn in Co(2 nm) / IrMn (50 nm). [54].

2.4.e Exchange bias between Dilute Magnetic Semiconductor and Antiferromagnetic Layer

To integrate DMSs into spintronic devices, an exchange-biasing scheme is quite important. Exchange coupling between a DMS ($Ga_{1-x}Mn_xAs$) and an antiferromagnet (MnO) has been reported [55].

$Ga_{1-x}Mn_xAs$ layers (x=0.08) were grown at 250℃ by low temperature molecular beam epitaxial on (001) epitaxial GaAs substrates. The magnetically active region of the sample consists of a 10-nm-thick $Ga_{1-x}Mn_xAs$ layer, capped with a thin Mn layer. To prepare the exchange-biased sample, the sample with Mn capping layer required a modest annealing cycle for a few minutes at ~ 200℃ during which the top Mn layer oxides to form MnO layer (T_N~118K)

Figure 2.29 (a) and 2.29 (b) depict two hysteresis loops for the GaMnAs (10nm) / MnO (4nm) bilayer, measured at T=10K after cooling the sample in a magnetic field of H=±2500 Oe. The loop offset of the hysteresis loops from the origin in a direction opposite to that of the cooling fields is a clear signature of exchange coupling in the bilayer.

Control measurements are used to rule out extrinsic effect : Fig. 2.29 (c) showed that cooling the sample in zero applied magnetic field results in a slightly baised hysteresis loop. The presence of some bias suggested that a small remnant magnetic field was present in the SQUID while cooling the sample. Figure 2.29 (d) showed that the exchange bias shift was absent in a sample of similar thickness and grown under identical conditions, but without the AFM overlayer. A notable increase of the coercive field for the Mn-capped sample compared to typical values for

uncapped samples, which is consistent with expected effects of exchange biasing.

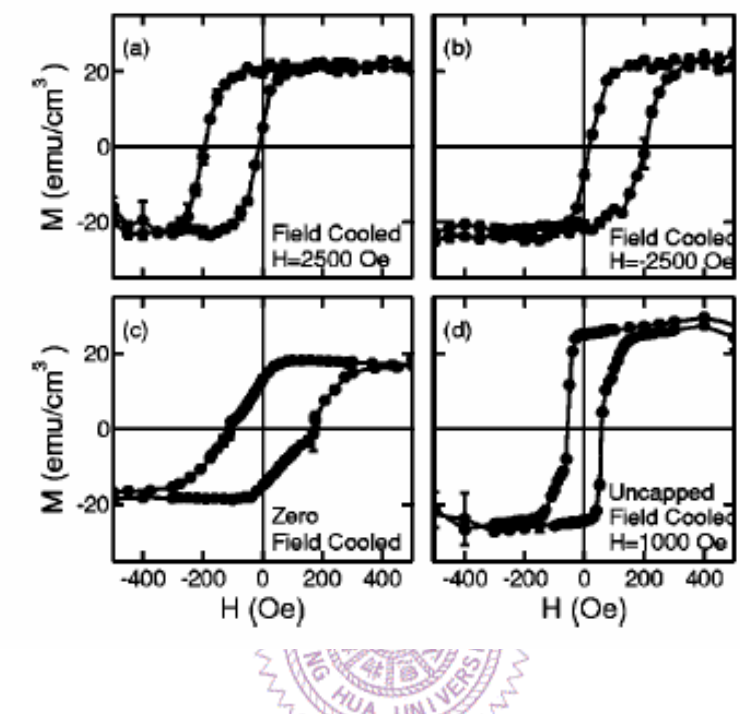

Fig. 2.29. Hysteresis loops of a GaMnAs (t=10nm) / MnO (t~4nm) bilayer measured at T=10K, after cooling in the presence of different magnetic fields: (a) H=2500 Oe, (b) H=-2500 Oe, and (c) H=0. In(d), we show the hysteresis loop measured at T=10K for an uncapped GaMnAs (t=15nm) control sample, after field cooling in H=1000 Oe. The diamagnetic and/or paramagnetic background has been subtracted from these hysteresis loops [55].

However, very limited work has been reported on the exchange bias of oxide-DMS systems. On the other hand, as we mentioned in the pervious section, the vertical magnetization shift obviously played an important role in investigating the exchange bias behavior. However, it is difficult to directly observe the vertical magnetization shift with conventional measured FM/AFM hysteresis loops. This is because the

typical magnetization of FM films is too large to reveal the existence of the pinned interfacial spins. Nevertheless, DMSs have much lower magnetization than typical FM films, which may enable us to investigate the role of the pinned spins in exchange-bias systems by measuring conventional hysteresis loops. In the chapter 5, we report both vertical and horizontal shifts in the hysteresis loops of ZnCoO/NiO bilayers measured with a superconducting quantum interference device (SQUID). We discuss the relationship between exchange-bias fields and the vertical magnetization shifts in the ZnCoO/NiO bilayers to elucidate the role of the pinned spins in the exchange-bias system